Engineering Transactions, **68**(1): 21–45, 2020, doi: 10.24423/EngTrans.1063.20200102
Polish Academy of Sciences • Institute of Fundamental Technological Research (IPPT PAN)
Université de Lorraine • Poznan University of Technology

Research Paper

Three-Dimensional Analysis of Laminated Plates with Functionally Graded Layers by Two-Dimensional Numerical Model

Piotr PLUCIŃSKI*, Jan JAŚKOWIEC

Cracow University of Technology
Faculty of Civil Engineering
Institute for Computational Civil Engineering
Warszawska 24, 31-155 Cracow, Poland
e-mail: j.jaskowiec@cce.pk.edu.pl
*Corresponding Author e-mail: p.plucinski@cce.pk.edu.pl

This work presents a three-dimensional (3D) numerical analysis of multi-layered laminated plates in which selected layers may be made of functionally graded material (FGM), in which the Young's modulus may change along the thickness as a consequence of a continuous and graded mixture of two materials. For the analysis, the method, known as FEM23, is applied, which uses a two-dimensional (2D) mesh, yet enables obtaining full 3D results for the layered structure. In FEM23, the layered structure may be a combination of thin and thick layers made of materials with significantly different properties. This paper presents two examples comparing the results to other numerical or analytical solutions. The examples confirm the correctness and flexibility of FEM23 for laminated plates with functionally graded layers.

Key words: functionally graded material; laminated plates; postprocessing; Finite Element Method; bending plate.

1. Introduction

The layered structures have been found to be very useful in a variety of engineering applications [4, 7, 9, 11, 34]. In particular, the sandwich plates have been widely used due to their high stiffness with respect to their weight. In recent years, functionally graded materials (FGM) in layered structures have drawn attention of many researchers [14, 16, 21, 30, 31]. These kinds of structures exhibit a high ability to withstand severe external conditions, such as high temperatures, chemical environments or impact forces, due to their continuous variation of material properties through their thickness [20, 23–25]. FGMs are the class of materials that consist of two or more constituents with different material prop-

erties. There are no strict boundaries between the two constituents, but the two materials are mixed. In FGMs, the desired properties in the required spatial direction can be obtained from the proportions of the constituents. The mechanical behaviour of the functionally graded layered structures has been at the forefront of interest of many researchers aiming to construct reliable numerical models.

Laminated plates are composed of layers of different materials which are stacked together. Some of the layers can be made of FGM, where the material properties change along their thickness. Many physical models have been developed for the analysis of laminated plates. For thin structures the equivalent laminate plate theory [8, 28] should be sufficiently accurate. The layerwise theories, in which independent degrees of freedom for each layer are applied, were introduced a few decades ago [2, 3, 5, 6, 29]. The layerwise theory provides a description of the displacement fields which is accurate for thin and thick laminate layers [3, 28]. Another approach to numerical analysis of the layered structures, called the sampling surface method, is presented in the works [15–19]. The formulation of the method is based on choosing a set of surfaces parallel to the shell's mid-surface. Appropriate degrees of freedom are introduced on the set of surfaces for a full 3D numerical analysis.

This work is focused on laminated plates where the layers can be made of FGM. The mechanical properties of FG materials change smoothly along their thickness. This allows them to maintain a high specific stiffness, in contrast to classical composites which have stress discontinuities at the layer-interfaces. A great number of theories have been proposed by researchers in order to properly describe the mechanical behaviour of FG materials [10, 22, 30]. A special kind of laminated plate, which is considered in this paper, is the sandwich plate. Typical sandwich plates consist of two faces, upper and lower thin layers, and a thick middle layer which is called the core, see Fig. 1. Most often the faces are made of a material with a high rigidity, while the core is low-weighted. The sandwich structures are very popular in design, as they allow a high rigidity with minimal weight. Additionally, each of these layers may be made of a FGM material.

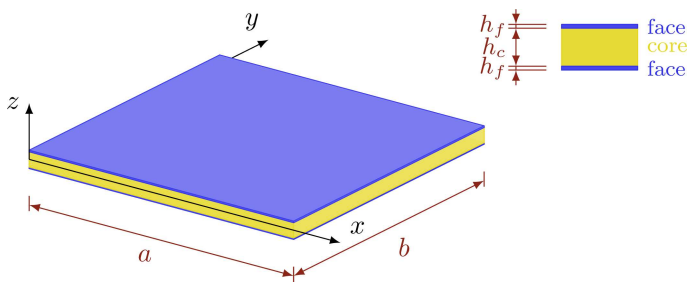

Fig. 1. The sandwich plate configuration and notations.

For a numerical simulation of the laminated plates, the method, called FEM23 (3D finite elements method on a 2D mesh), is applied in this paper, see [12, 13]. FEM23 uses only a 2D finite element mesh, but a full 3D analysis is performed for the multi-layered plates. In the method, the degrees of freedom along the plate thickness are gathered at the mesh nodes. Note that the degrees of freedom of this type were proposed in the work of Szabó and Sahrmann [32] for the so called hierarchic plate and shell models based on p-extension. Such degrees of freedom, called the through-thickness dofs, were then further developed, justified and applied in numerous works of Zboiński [36, 38, 39] concerning the development of the 3D-based hierarchical plate and shell models. We extended the same approach for the multilayered structures composed of layers of various material properties, including FGM. What is also original in our approach is the application of integration through the thickness performed before the in-plane approximation of the displacement field. Such integration allows taking extremely thin layers into account. A special anisotropic spatial approximation is applied in FEM23 as a cross product of in-plane and transverse approximations [35, 37, 40]. The anisotropic approximation for standard 3D analysis has been also applied in [1, 26, 27].

Using a special postprocessing procedure, the full 3D results may be presented. FEM23 can be applied for homogeneous plates, as well as for multi-layered plates, in which the thin layers may be combined with thick ones. In this paper, the use of FEM23 is extended to layers made of FGMs in which the Young's modulus changes along thickness. In this paper, FEM23 is presented first for a single-layer FGM plate, which afterwards, is generalized for a multi-layered FGM plate. In FEM23, the in-plane finite element mesh can be made of triangular or quadrilateral elements. The spatial approximation is a combination of 2D in-plane and 1D transverse approximations where the orders of the two approximations are independent of each other. Additionally, the orders of transverse approximation for each layer can be chosen according to their thicknesses. For very thin layers, the first order is sufficient, while for thick layers, a third or fourth order transverse approximation needs to be applied. Figure 2 illustrates

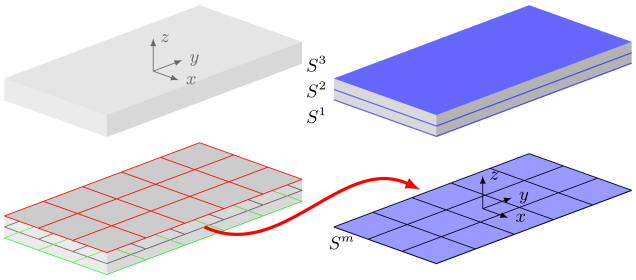

Fig. 2. Concept of in-plane 2nd order transverse approximation for one layer. Three surfaces are denoted: upper S^3, lower S^1 and middle S^2.

the concept of the in-plane mesh and the 2nd order transverse approximation for a single layered plate. In the plate, three surfaces can be distinguished: lower, upper, and mid surface. Each of the surfaces is discretized by a 2D mesh. The three meshes are the same, so they can be identified by only the single, in-plane mesh. In this situation, the vector of degrees of freedom at a single node consists of displacements on the three surfaces. For a multi-layered plate, an appropriate approximation is prepared for each of the layers. Subsequently, an extended assembling procedure is applied to obtain a discrete system of equations for the multi-layered plate.

This paper is focused on the numerical modelling of multi-layered FG plates. The approach is presented first for a single-layered plates, and then it is extended to multi-layered structures. The mathematical model for FEM23, derived for a single-layered FG plate is presented in Sec. 2. The in-plane approximation, based on a 2D in-plane finite mesh with standard shape function but including transverse approximation, is described in Sec. 3. Section 4 presents the extension of FEM23 into multi-layered plates. The FEM23 finite elements are presented in more details in Sec. 5. Post-processing procedures are described in Sec. 6. Section 7 presents numerical examples where the bending of multi-layered FG plates is analysed. The paper ends with several conclusions.

2. Mathematical model

As mentioned in the introduction, we first present modeling of a single-layered FG plate and, subsequently, extend it to a multi-layered plate by special assembling procedure. The mathematical model for a single layer of FG material with appropriate boundary conditions has the well-known weak form

$$\int\limits_{S^\sigma} \mathbf{v}\cdot\widehat{\mathbf{t}}\,\mathrm{d}S - \int\limits_{V} \boldsymbol{\varepsilon}(\mathbf{v}) : \boldsymbol{\sigma}\,\mathrm{d}V = 0, \qquad \mathbf{u} = \widehat{\mathbf{u}} \quad \text{on } S^u, \tag{2.1}$$

where $\mathbf{v}$ is a test function with condition $\mathbf{v} = \mathbf{0}$ on S^u, $\boldsymbol{\sigma}$ is the stress tensor, $\widehat{\mathbf{t}}$ is the prescribed traction forces vector, S^σ is the part of the boundary where tractions $\widehat{\mathbf{t}}$ are prescribed, $\mathbf{u}$ is the displacement vector, $\widehat{\mathbf{u}}$ is the prescribed displacement vector, S^u is the part of the boundary where displacement $\widehat{\mathbf{u}}$ is prescribed. The equation does not take into account the action of body forces, but the generality of the model does not suffer. The Bubnow-Galerkin approach is used in this paper, so both the trail and test functions will use the same approximation fields.

Equation (2.1) is completed by Cauchy strain tensor and the constitutive Hooke's law

$$\boldsymbol{\varepsilon}(\mathbf{u}) = \boldsymbol{\nabla}_s\mathbf{u} = \frac{1}{2}\Big(\boldsymbol{\nabla}\mathbf{u} + (\boldsymbol{\nabla}\mathbf{u})^{\mathrm{T}}\Big), \qquad \boldsymbol{\sigma}(\mathbf{u}) = \mathbf{E}(z) : \boldsymbol{\varepsilon}(\mathbf{u}), \tag{2.2}$$

where Hooke's tensor is changing along coordinate z, namely along the plate's thickness. Hooke's tensor can be expressed

$$\mathbf{E}(z) = \lambda(z)\mathrm{I} \otimes \mathrm{I} + 2\mu(z)\mathrm{II}, \quad (\mathbf{E})_{ijkl} = \lambda(z)\,\delta_{ij}\delta_{kl} + \mu(z)\,(\delta_{ik}\delta_{jl} + \delta_{il}\delta_{jk}), \tag{2.3}$$

where $\mu(z)$ and $\lambda(z)$ are Lame material parameters that vary along the plate thickness, I is the second-rank identity tensor, and II is the symmetric part of the fourth-rank identity tensor.

In the FEM23 it is much convenient to deal with full displacement gradient instead of the Cauchy strain tensor. Thus, it can be shown that the Eq. (2.1) can be rewritten to the following form

$$\int\limits_{S^\sigma} \mathbf{v} \cdot \widehat{\mathbf{t}}\,\mathrm{d}S - \int\limits_{V} \boldsymbol{\nabla}\mathbf{v} : \mathbf{E}(z) : \boldsymbol{\nabla}\mathbf{u}\,\mathrm{d}V = 0, \qquad \mathbf{u} = \widehat{\mathbf{u}} \quad \text{on } S^u. \tag{2.4}$$

As mentioned in the introduction, the spatial approximation of the displacement vector will be a combination of the 2D in-plane approximation and the 1D transverse approximation. Thus, Eq. (2.1) needs to be rewritten so as to distinguish between transverse and in-plane derivatives

$$\boldsymbol{\nabla}\mathbf{u} = \left[\overline{\boldsymbol{\nabla}}\mathbf{u} \quad \frac{\partial \mathbf{u}}{\partial z}\right], \qquad \overline{\boldsymbol{\nabla}}\mathbf{u} = \begin{bmatrix} \dfrac{\partial u_x}{\partial x} & \dfrac{\partial u_x}{\partial y} \\ \dfrac{\partial u_y}{\partial x} & \dfrac{\partial u_y}{\partial y} \\ \dfrac{\partial u_z}{\partial x} & \dfrac{\partial u_z}{\partial y} \end{bmatrix}. \tag{2.5}$$

This technique will help to reduce the numerical model to a 2D in-plane space, while keeping a full 3D physical description. Due to the fact that the plate is flat and its thickness is constant, all volume integrals can be expressed by the combination of two integrals: the 2D integral over mid-surface S^m and the 1D integral along the plate thickness. The weak formulation, after such modifications has the form:

$$\begin{aligned} \int\limits_{S^m} \int\limits_{-h/2}^{h/2} \frac{\partial \mathbf{v}}{\partial z} \cdot \mathbf{E}_1(z) \cdot \frac{\partial \mathbf{u}}{\partial z}\,\mathrm{d}z\,\mathrm{d}S + \int\limits_{S^m} \int\limits_{-h/2}^{h/2} \left(\frac{\partial \mathbf{v}}{\partial z} \cdot \mathbf{E}_2(z) : \overline{\boldsymbol{\nabla}}\mathbf{u}\right)\mathrm{d}z\,\mathrm{d}S \\ + \int\limits_{S^m} \int\limits_{-h/2}^{h/2} \left(\overline{\boldsymbol{\nabla}}\mathbf{v}^{\mathrm{T}} : \mathbf{E}_3(z) \cdot \frac{\partial \mathbf{u}}{\partial z}\right)\mathrm{d}z\,\mathrm{d}S \\ + \int\limits_{S^m} \int\limits_{-h/2}^{h/2} \overline{\boldsymbol{\nabla}}\mathbf{v}^{\mathrm{T}} : \mathbf{E}_4(z) : \overline{\boldsymbol{\nabla}}\mathbf{u}\,\mathrm{d}z\,\mathrm{d}S = \int\limits_{S^\sigma} \mathbf{v} \cdot \widehat{\mathbf{t}}\,\mathrm{d}S, \end{aligned} \tag{2.6}$$

where h is the plate thickness, S^m is the in-plane surface. The tensors $\mathbf{E}_i$, $i = 1, ..., 4$ are the appropriate parts of Hooke's tensor, which come directly from the gradient decomposition shown in Eq. (2.5). Their definitions are as follows where the z parameter is skipped in notation for the sake of clarity

$$(\mathbf{E}_1)_{11} = (\mathbf{E}_1)_{22} = \mu, \qquad (\mathbf{E}_1)_{33} = 2\mu + \lambda, \tag{2.7}$$

$$(\mathbf{E}_2)_{131} = \mu, \qquad (\mathbf{E}_2)_{232} = \mu, \qquad (\mathbf{E}_2)_{311} = \lambda, \qquad (\mathbf{E}_2)_{322} = \lambda, \tag{2.8}$$

$$\mathbf{E}_3 = \mathbf{E}_2^{\mathrm{T}} \quad \Rightarrow \quad (\mathbf{E}_3)_{ijk} = (\mathbf{E}_2)_{kji}, \tag{2.9}$$

$$\begin{aligned} &(\mathbf{E}_4)_{1111} = (\mathbf{E}_4)_{2222} = 2\mu + \lambda, \\ &(\mathbf{E}_4)_{1122} = (\mathbf{E}_4)_{2211} = \lambda, \\ &(\mathbf{E}_4)_{1212} = (\mathbf{E}_4)_{1221} = (\mathbf{E}_4)_{2121} = (\mathbf{E}_4)_{2112} = (\mathbf{E}_4)_{3131} = (\mathbf{E}_4)_{3232} = \mu. \end{aligned} \tag{2.10}$$

The transverse integrals along the plate thickness h are substituted through implicit numerical integration using the Gauss-Legendre quadrature of appropriate order

$$\int_{-h/2}^{h/2} g(x, y, z)\, \mathrm{d}z = \sum_{i}^{n_g} w_i\, g(x, y, z_i), \tag{2.11}$$

where $g(x, y, z)$ is an auxiliary integrand, n_g is the number of integration points, z_i and w_i are z-coordinate of the i-th integration point and the integration weight corresponding to the point, respectively. The implicit numerical integration has been successfully applied in papers [12, 13] where the integration schemes are described in details. The transverse quadrature order needs to be chosen so as to account for the transverse approximation order, as well as the changing of Hooke's tensor. Finally, the weak form of the considered problem uses only 2D integrals for a full 3D model

$$\begin{aligned} &\int_{S^m} \sum_{i}^{n_g} w_i \left(\frac{\partial \mathbf{v}}{\partial z} \cdot \mathbf{E}_1(z) \cdot \frac{\partial \mathbf{u}}{\partial z} \right)\Bigg|_{z=z_i} \mathrm{d}S \\ &+ \int_{S^m} \sum_{i}^{n_g} w_i \left(\frac{\partial \mathbf{v}}{\partial z} \cdot \mathbf{E}_2(z) : \overline{\boldsymbol{\nabla}} \mathbf{u} \right)\Bigg|_{z=z_i} \mathrm{d}S + \int_{S^m} \sum_{i}^{n_g} w_i \left(\overline{\boldsymbol{\nabla}} \mathbf{v}^{\mathrm{T}} : \mathbf{E}_3(z) \cdot \frac{\partial \mathbf{u}}{\partial z} \right)\Bigg|_{z=z_i} \mathrm{d}S \\ &\qquad + \int_{S^m} \sum_{i}^{n_g} w_i \left(\overline{\boldsymbol{\nabla}} \mathbf{v}^{\mathrm{T}} : \mathbf{E}_4(z) : \overline{\boldsymbol{\nabla}} \mathbf{u} \right)\Big|_{z=z_i} \mathrm{d}S = \int_{S^\sigma} \mathbf{v} \cdot \widehat{\mathbf{t}}\, \mathrm{d}S. \end{aligned} \tag{2.12}$$

For effective calculation of the integrals in Eq. (2.12) the both trial and test functions are going to be decomposed so that to distinguish the z direction from the xy plane. Then, it is quite easy to apply the inner summations so that to exclude the z parameter. Such decomposition is presented in the following section.

3. Approximation

The details concerning the spatial approximation have already been presented in work [13]. This paper presents an outline of the approximation scheme. The spatial approximation of the displacement is a combination of the in-plane approximation and the transverse one. Displacement $\mathbf{u}(x, y, z)$, using the 1D transverse approximation along the plate thickness, is expressed the following way:

$$\mathbf{u}(x, y, z) = \sum_{i=1}^{nS} N_i(z)\mathbf{u}^i(x, y), \tag{3.1}$$

where nS is the number of surfaces specified along thickness, which strongly depends on the order of the transverse approximation, N_i is the i-th Lagrange polynomial of the appropriate $nS - 1$ order, $\mathbf{u}^i(x, y)$ is the displacement vector on the i-th surface. The same kind of the displacement decomposition has been priorly proposed in [32, 36] for hierarchical shell models. In a case of thin plate, usually the first order transverse approximation is enough, then the number of surfaces is $nS = 2$. When the plate is thick the second or third approximation order should be applied with $nS = 3$ and $nS = 4$, respectively. The choice of the transverse approximation order should also depend on the kind of material, i.e. for the FG plates the order should be appropriately higher. Some numerical study highlighting the reason for selecting a the transverse approximation order has been presented in [13].

On the other hand, every vector $\mathbf{u}^i(x, y)$ is approximated using shape functions in turn using one single in-plane 2D mesh

$$\mathbf{u}^i(x, y) = \mathbf{\Phi}(x, y)\check{\mathbf{u}}^i, \tag{3.2}$$

where $\mathbf{\Phi}(x, y)$ is the approximation matrix defined on a 2D in-plane mesh and $\check{\mathbf{u}}^i$ is the vector of nodal displacements on the i-th surface.

Using Eqs (3.1) and (3.2) the displacement vector in the entire domain can be approximated as follows:

$$\begin{aligned} \mathbf{u}(x, y, z) &= \begin{bmatrix} N_1(z)\mathbf{\Phi}(x, y) & N_2(z)\mathbf{\Phi}(x, y) & \dots & N_{nS}(z)\mathbf{\Phi}(x, y) \end{bmatrix} \check{\mathbf{u}} \\ &= \mathbf{\Psi}(x, y, z)\check{\mathbf{u}}, \end{aligned} \tag{3.3}$$

where the global vector of degrees of freedom $\check{\mathbf{u}}$ consists of the vectors associated with subsequent surfaces

$$\check{\mathbf{u}} = \begin{bmatrix} \check{\mathbf{u}}^1 \\ \check{\mathbf{u}}^2 \\ \vdots \\ \check{\mathbf{u}}^{nS} \end{bmatrix}. \tag{3.4}$$

The vector of degrees of freedom defined this way is exactly the same as the corresponding vector of the through-thickness degrees of freedom of the 3D-based hierarchical shell models (see [38, 39]).

In the spatial approximation (Eq. (3.3)) the direct distinguishing of the transverse and in-plane directions is established. Thus, the derivatives in these directions must be evaluated separately

$$\begin{aligned} \overline{\boldsymbol{\nabla}}\mathbf{u}(x,y,z) &= \left[N_1(z)\overline{\boldsymbol{\nabla}}\boldsymbol{\Phi}(x,y) \;\; N_2(z)\overline{\boldsymbol{\nabla}}\boldsymbol{\Phi}(x,y) \;\; \ldots \;\; N_{nS}(z)\overline{\boldsymbol{\nabla}}\boldsymbol{\Phi}(x,y)\right]\check{\mathbf{u}} \\ &= \overline{\boldsymbol{\nabla}}\boldsymbol{\Psi}(x,y,z)\check{\mathbf{u}}, \\ \frac{\partial \mathbf{u}}{\partial z}(x,y,z) &= \left[N_1'(z)\boldsymbol{\Phi}(x,y) \;\; N_2'(z)\boldsymbol{\Phi}(x,y) \;\; \ldots \;\; N_{nS}'(z)\boldsymbol{\Phi}(x,y)\right]\check{\mathbf{u}} \\ &= \boldsymbol{\Psi}_{,z}(x,y,z)\check{\mathbf{u}}. \end{aligned} \tag{3.5}$$

After substituting the approximation shown in Eq. (3.3) and derivatives, Eq. (3.5), to Eq. (2.12), the discrete system of equation is obtained

$$(\mathbf{K}_1 + \mathbf{K}_2 + \mathbf{K}_3 + \mathbf{K}_4)\,\check{\mathbf{u}} = \mathbf{F}, \tag{3.6}$$

where particular matrices and the right hand-side vector are defined as follows:

$$\begin{aligned} \mathbf{K}_1 &= \sum_i^{n_g} w_i \int_{S^m} \boldsymbol{\Psi}_{,z}(x,y,z_i)\cdot\mathbf{E}_1(z_i)\cdot\boldsymbol{\Psi}_{,z}(x,y,z_i)\,\mathrm{d}S, \\ \mathbf{K}_2 &= \sum_i^{n_g} w_i \int_{S^m} \boldsymbol{\Psi}_{,z}(x,y,z_i)\cdot\mathbf{E}_2(z_i) : \overline{\boldsymbol{\nabla}}\boldsymbol{\Psi}(x,y,z_i)\,\mathrm{d}S, \qquad \mathbf{K}_3 = \mathbf{K}_2{}^{\mathrm{T}}, \\ \mathbf{K}_4 &= \sum_i^{n_g} w_i \int_{S^m} \overline{\boldsymbol{\nabla}}\boldsymbol{\Psi}^{\mathrm{T}}(x,y,z_i) : \mathbf{E}_4(z_i) : \overline{\boldsymbol{\nabla}}\boldsymbol{\Psi}(x,y,z_i)\,\mathrm{d}S, \\ \mathbf{F} &= \int_{S^\sigma} \boldsymbol{\Psi}^{\mathrm{T}}(x,y,z_\sigma)\cdot\widehat{\mathbf{t}}\,\mathrm{d}S, \end{aligned} \tag{3.7}$$

where z_σ is the level on which traction $\widehat{\mathbf{t}}$ is applied.

4. Multi-layered structure

The previous sections, namely Secs 2 and 3, present an analysis for a single-layer plate. The approach can be quite easily extended for multi-layered plates, using the extended assembling procedure. The two neighbouring layers share the same set of nodes, on the lower and upper surface, respectively. To assemble the stiffness matrices for the two layers the components associated with the common degrees of freedom are added together in the global stiffness matrix. It is repeated for each layer in the structure. A multi-layer plate consists of M layers which are numbered sequentially starting from the lower layer. One single layer is made of material λ_i and μ_i parameters which may change along its thickness. Each layer may have a different thickness, defined as h_i, and so the approximation order may be different for each of the layers. The vector of degrees of freedom for single i-th layer may be described as follows:

$$\check{\mathbf{u}}^{(i)} = \begin{bmatrix} \check{\mathbf{u}}^{(i)1} \\ \check{\mathbf{u}}^{(i)2} \\ \vdots \\ \check{\mathbf{u}}^{(i)nS} \end{bmatrix}. \tag{4.1}$$

Two neighbouring layers, which adhere to each other, share the surface and, consequently, the degrees of freedom on the surface. The common degrees of freedom satisfy the relation:

$$\check{\mathbf{u}}^{(i)nS} = \check{\mathbf{u}}^{(i+1)1}. \tag{4.2}$$

The system of equations for each layer (3.6) is assembled, keeping in mind relation (4.2), into a global system of equations for the multi-layer plate

$$(\mathbf{K}_1 + \mathbf{K}_2 + \mathbf{K}_3 + \mathbf{K}_4)\,\check{\mathbf{u}} = \mathbf{F}. \tag{4.3}$$

The global system of Eq. (4.3) has the same structure as Eq. (3.6), but now the matrices and vector are the results of the assembling the procedure

$$\mathbf{K}_n = \sum_i^N \mathbf{A}^{i\mathrm{T}} \mathbf{K}_n^i \mathbf{A}^i, \qquad \mathbf{F} = \sum_i^N \mathbf{A}^{i\mathrm{T}} \mathbf{F}^i, \tag{4.4}$$

where $\mathbf{A}^i$ is the assembling operator for the i-th layer, $\mathbf{K}_n^i$ is the n-th matrix for the i-th layer, and $\mathbf{F}^i$ is the right hand-side vector for the i-th layer. It is worth emphasising that the discretization of surfaces S^m for each of the layers is the same, and this explains why S^m is assumed to be the middle surface of the entire layered plate.

5. Finite element

In FEM23, only 2D in-plane finite elements are applied, although a full 3D approximation is applied to these elements, see Eq. (3.3). It means that each node in the finite element has to keep the degrees of freedom (displacements) gathered along the thickness of each layer. It is illustrated in Fig. 3 which presents the example of a transverse second order single layer approximation. In this case the single node keeps nine displacements altogether: the displacements – of the lower, middle and upper surfaces, respectively. When a multi-layer structure is analysed, the degrees of freedom from all the layers are assembled and kept in the single node. For example, when the structure consists of four layers and the second order transverse approximation has been chosen for each layer then there are 27 degrees of freedom in each node. The layer stiffness matrix from Eqs (3.6) and (3.7), require in-plane and transverse integrations. In the transverse direction the 1D Gauss integration is performed while the in-plane the 2D integration schemes in the elements is performed. The global stiffness matrix consists of assembled layer stiffness matrices, that is shown in Eq. (4.4).

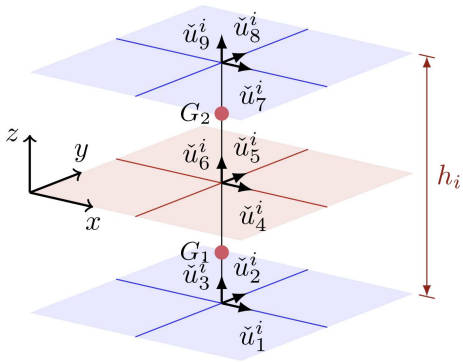

Fig. 3. Set of degrees of freedom for the i-th noded 2D finite elements in FEM23 for the 2nd order transverse approximation and two integration points G_1 and G_2.

The presented approach is very flexible, since the analysis may be limited to only 2D finite elements yet, implementing a full 3D approximation. Figure 4 presents sets of 2D finite elements applied in FEM23. The in-plane approxi-

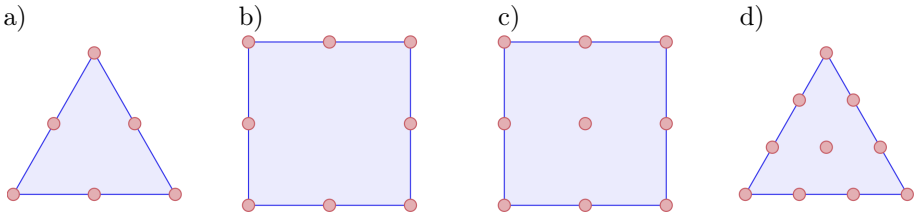

Fig. 4. 2D finite elements applied in FEM23: a) 6-noded, b) 8-noded, c) 9-noded, d) 10-noded.

mation order in FEM23 is taken from the 2D finite element order, while the transverse approximation order in the layers can be set independently of the orders of elements. It makes this approach very flexible since calculations may be performed for various approximation orders but for the same mesh.

6. Postprocessing

After solving the linear system of equations described by Eq. (4.3), the global displacements vector becomes known. The vectors associated with particular layers can be easily extracted from the global vector. Using the procedure described in work [13], the structure can be shown as a 3D deformed multi-layer structure. The visualisation of the 3D solution is presented using VTK graphics, which use tetrahedrons for a 3D representation of the domain. The visualisation of the stress distribution may need another approach, since it may require applying a smoothing procedure. To obtain a smooth stress distribution, the well-known Zienkiewicz-Zhu (ZZ) technique can be used [41, 42]. In context of this work, the ZZ technique needs to be adapted in such a way so as to take into account the special spatial approximation, the multi-layer structure, and the functionally graded material in the layers.

The stress tensor may be obtained directly from the spatial approximation using the in-plane gradient and transverse derivative. The stress components can be written in the following uniform manner

$$\sigma_{ij} = \mathbf{E}_{xy}^{(ij)}(z) : \overline{\boldsymbol{\nabla}}\boldsymbol{\Psi}\check{\mathbf{u}} + \mathbf{E}_{z}^{(ij)}(z) \cdot \boldsymbol{\Psi}_{,z}\,\check{\mathbf{u}} \qquad \text{for} \quad i,j = x,y,z, \tag{6.1}$$

where $\mathbf{E}_{xy}^{(ij)}(z)$ and $\mathbf{E}_{z}^{(ij)}(z)$ are proper parts of Hooke's tensor which definitions come directly from the decomposition in Eq. (2.5) and reduction to the ij component. Their definitions are as follows:

$$\mathbf{E}_{xy}^{(xx)} = \begin{bmatrix} (2\mu+\lambda) & 0 \\ 0 & \lambda \\ 0 & 0 \end{bmatrix}, \qquad \mathbf{E}_{z}^{(xx)} = \begin{bmatrix} 0 & 0 & \lambda \end{bmatrix}, \tag{6.2}$$

$$\mathbf{E}_{xy}^{(yy)} = \begin{bmatrix} \lambda & 0 \\ 0 & (2\mu+\lambda) \\ 0 & 0 \end{bmatrix}, \qquad \mathbf{E}_{z}^{(yy)} = \begin{bmatrix} 0 & 0 & \lambda \end{bmatrix}, \tag{6.3}$$

$$\mathbf{E}_{xy}^{(zz)} = \begin{bmatrix} \lambda & 0 \\ 0 & \lambda \\ 0 & 0 \end{bmatrix}, \qquad \mathbf{E}_{z}^{(zz)} = \begin{bmatrix} 0 & 0 & (2\mu+\lambda) \end{bmatrix}, \tag{6.4}$$

$$\mathbf{E}_{xy}^{(xy)} = \begin{bmatrix} 0 & \mu \\ \mu & 0 \\ 0 & 0 \end{bmatrix}, \qquad \mathbf{E}_{z}^{(xy)} = \begin{bmatrix} 0 & 0 & 0 \end{bmatrix}, \tag{6.5}$$

$$\mathbf{E}_{xy}^{(xz)} = \begin{bmatrix} 0 & 0 \\ 0 & 0 \\ \mu & 0 \end{bmatrix}, \qquad \mathbf{E}_{z}^{(xz)} = \begin{bmatrix} \mu & 0 & 0 \end{bmatrix}, \tag{6.6}$$

$$\mathbf{E}_{xy}^{(yz)} = \begin{bmatrix} 0 & 0 \\ 0 & 0 \\ 0 & \mu \end{bmatrix}, \qquad \mathbf{E}_{z}^{(yz)} = \begin{bmatrix} 0 & \mu & 0 \end{bmatrix}. \tag{6.7}$$

Since the derivatives of the finite element approximation are discontinuous, the stresses in Eq. (6.1) are also discontinuous. The ZZ smoothing technique is applied to make the stresses field smooth. The ZZ procedure is based on the least squares approach, in which all continuous stress components σ_{ij}^{*} must be found through the minimisation of the following error:

$$\epsilon_{ij} = \int\limits_{V} \left(\sigma_{ij}^{*} - \sigma_{ij}\right)^{2} \mathrm{d}V. \tag{6.8}$$

Stress σ_{ij}^{*} is approximated in the domain in the same way as the displacement in Eq. (3.3), i.e.

$$\begin{aligned} \sigma_{ij}^{*} &= \left[N_1(z)\mathbf{\Phi}^{\sigma}(x,y) \;\; N_2(z)\mathbf{\Phi}^{\sigma}(x,y) \ldots \;\; N_{nS}(z)\mathbf{\Phi}^{\sigma}(x,y)\right] \check{\mathbf{u}} \\ &= \mathbf{\Psi}^{\sigma}(x,y,z)\check{\boldsymbol{\sigma}}_{ij}, \end{aligned} \tag{6.9}$$

where $\mathbf{\Phi}^{\sigma}$ is the appropriate approximation matrix composed of the same shape functions as for displacements, $\check{\boldsymbol{\sigma}}_{ij}$ is the vector of degrees of freedom for the ij stress component. After minimisation of Eq. (6.8), we obtain a linear system of equations where the stress degrees of freedom can be calculated

$$\mathbf{M}^{\sigma}\check{\boldsymbol{\sigma}}_{ij} = \mathbf{F}_{ij}^{\sigma}, \tag{6.10}$$

where

$$\begin{aligned} \mathbf{M}^{\sigma} &= \int\limits_{S^m} \sum_{i}^{n_g} w_i \left(\mathbf{\Psi}^{\sigma\mathrm{T}}\mathbf{\Psi}^{\sigma}\right)\Big|_{z=z_i} \mathrm{d}S, \\ \mathbf{F}_{ij}^{\sigma} &= \int\limits_{S^m} \sum_{i}^{n_g} w_i \left(\mathbf{\Psi}^{\sigma\mathrm{T}}\mathbf{E}_{z}^{(ij)} \cdot \mathbf{\Psi}_{,z}\right)\Big|_{z=z_i} \mathrm{d}S\, \check{\mathbf{u}} \\ &\quad + \int\limits_{S^m} \sum_{i}^{n_g} w_i \left(\mathbf{\Psi}^{\sigma\mathrm{T}}\mathbf{E}_{z}^{(ij)} \cdot \mathbf{\Psi}_{,z}\right)\Big|_{z=z_i} \mathrm{d}S\, \check{\mathbf{u}}. \end{aligned} \tag{6.11}$$

The Eq. (6.10) is prepared for each of the stress tensor components, six altogether. For the multi-layer structure the equations are prepared for each layer independently. For example, in a case of three-layered structure 18 system of equations need to be prepared and solved. The number of unknown in this equation is three times smaller in comparison to the main system of equation for the single layer in Eq. (3.6).

7. Examples

In this section, two numerical examples are presented to show the efficiency and accuracy of FEM23. The meshes in the examples consist of 2D quadrilateral 9-noded finite elements. For thin layers, the first order of transverse approximation has been chosen, while for thick layers the fourth order must to be used.

In the first example, we consider a simply supported sandwich beam, loaded at the top surface. In the first case, the core is made of a homogeneous material, while in the second case, the core is made of FGM. The other example involves square plates. The homogeneous, as well as metal-ceramic FGM plates, are analysed using FEM23. The results are compared with those obtained by the ABAQUS package or those taken from literature.

7.1. The sandwich beam with constant material properties

In this example, a 3D analysis of a simply supported sandwich beam has been performed. The beam is subjected to a constant load applied to the upper surface $p_z = 1$ Pa. The geometry and boundary conditions are shown in Fig. 5. In this example the results from FEM23 are compared with the results obtained from the standard full 3D FEM (ABAQUS) analysis and with the results based on various beam models [10]. Two cases of a sandwich beam are considered. In the first case the faces and the core are homogeneous, and in the second the core is made of FGM in which the Young's modulus is changing along the core thickness.

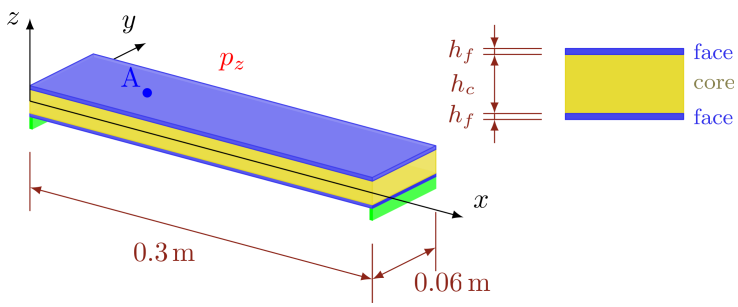

Fig. 5. Configuration of a rectangular sandwich plate – example 1.

In the first case, both the face and core consist of homogeneous and isotropic materials with the following material properties: $E_f = 50$ GPa, $\nu = 0.25$, $E_c = 500$ MPa and $\nu = 0.35$. The thickness of the core and face are assumed to be: $h_c = 20$ mm and $h_f = 0.3$ mm, respectively.

This example has been solved by FEM23 and, for comparison, in a commercial program SIMULIA Abaqus FEA. In Abaqus a full 3D analysis has been performed using 2nd order 3D finite elements. For a full 3D analysis in Abaqus, the following sizes of finite elements have been assumed: $5 \times 5 \times 5$ mm for the core and $5 \times 5 \times 0.3$ mm for the faces. In FEM23, planar 7.5×7.5 mm finite elements have been applied.

The results, in the form of maps of stress σ_x and displacement u_z on the deformed structure are presented in Fig. 6. The results obtained by FEM23 and Abaqus are in great agreement. The values of the displacements and stresses obtained from the two approaches are nearly the same. In both results, the stresses are concentrated on the faces, whereas the values of stresses in the core are one hundred times smaller, a typical situation for sandwich structures. The example has been calculated once again using the FEM23, but using second order transverse approximation in the sandwich faces. There were no noticeable differences with the previous results. That indicates that first order transverse approximation for thin layers is sufficient.

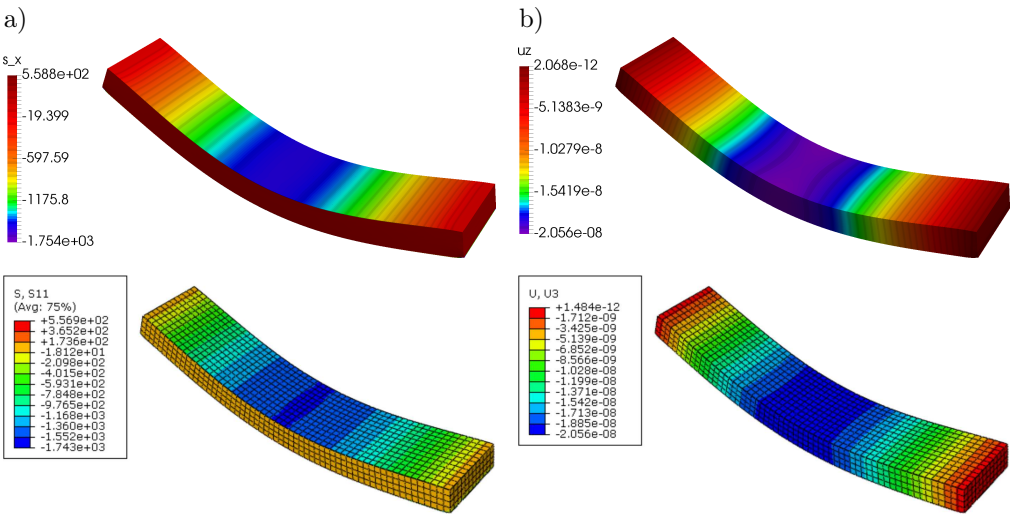

FIG. 6. Maps of stress σ_x [Pa]: a) and displacement u_z [m], b) obtained by FEM23 and Abaqus – example 1.

In the second case of this example, we considered the core made of FGM. In the core, Young's modulus E_c is changing along its thickness. Following work [10], two schemes for E_c are assumed, which are shown in Fig. 7. In paper [10], various

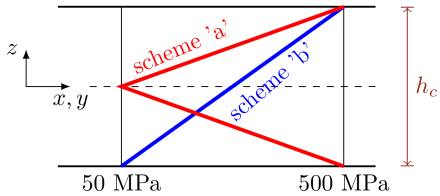

FIG. 7. Two schemes of E_c variation for sandwich beam – example 1.

beam models are used for a numerical analysis of the sandwich beam. In order to compare the full 3D results by FEM23 with those obtained by the beam models, in FEM23 the beam is supported at half of the beam thickness. Such a support is not realistic, but is closer to the one-dimensional beam model.

Due to the fact that Young's modulus in the scheme 'b' varies along the core thickness the transverse quadrature for numerical integration has been increased to five in the core. In the scheme 'a', the function of E_c is a broken function, so the core layer has been split into two sub-layers for correct transverse numerical integration. Two kinds of loading on the upper surface are applied: (i) uniform pressure $p_z = 1$ Pa for scheme 'a' and (ii) sinusoidal pressure $p_z = \sin\left(\frac{\pi y}{0.3}\right)$ Pa for scheme 'b'.

The results for the core, in terms of displacements u_x and u_y and stresses σ_{xx} along the core thickness at point A (in the middle of the beam width and at one quarter of the beam length), are shown in Figs 8–10. The results obtained by FEM23 are put together with those presented in work [10].

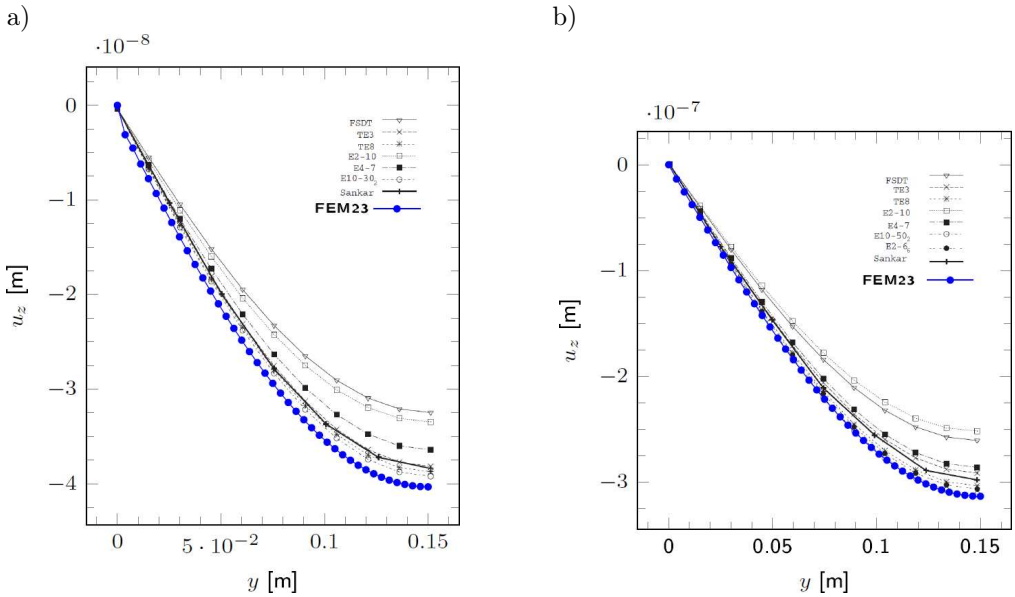

FIG. 8. Transverse displacement along the beam axis: scheme 'a' (a) and scheme 'b' (b) – example 1.

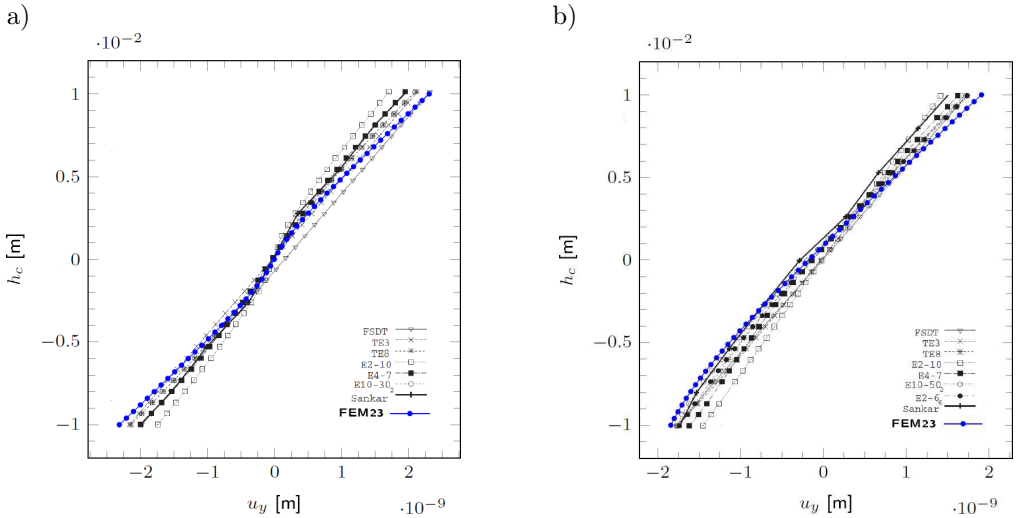

FIG. 9. Axial displacement along the core thickness: scheme 'a' (a) and scheme 'b' (b) – example 1.

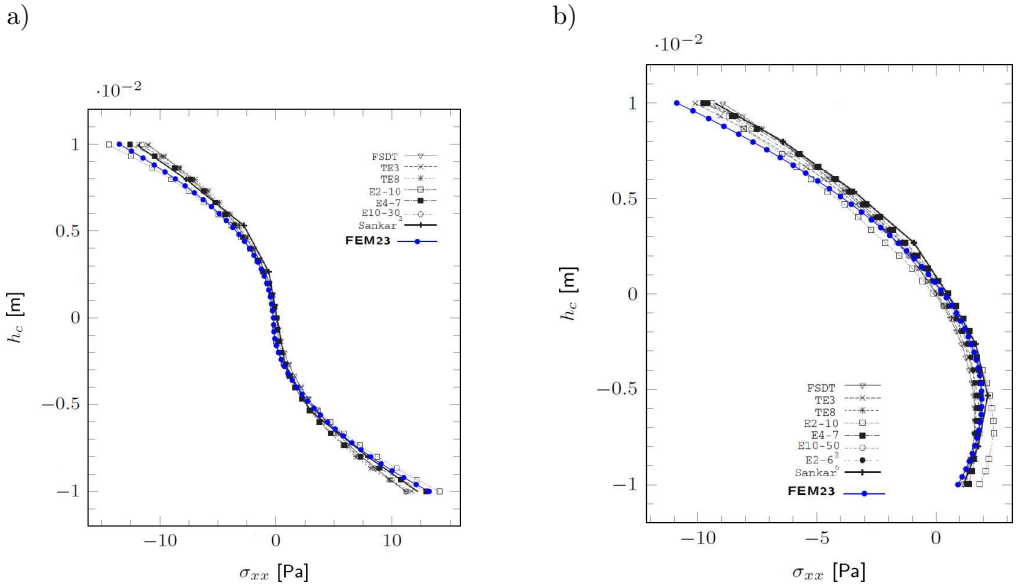

FIG. 10. Axial stress σ_{xx} along the core thickness: scheme 'a' (a) and scheme 'b' (b) – example 1.

It can be noticed that the FEM23 results are very close to those obtained using various beam models. The differences in the results origin from model dimensions, i.e. the FEM23 uses a 3D model while the beam models are one-dimensional.

7.2. Bending of square plate

In this example, bending of a square plate is analysed. Two types of boundary conditions are considered: simply supported "SSSS" and clamped "CCCC" all over the outer boundary. Three types of plates are analysed: one homogeneous and two made of graded materials. The three types of transverse structures of the plates are shown in Fig. 11. In the type A, the plate is made uniformly of metal. The plate of type B consists of a single FG layer. In the plate of type C, three layers are distinguished: the two outer layers are metal-ceramic FGM and the inner layer is homogeneous ceramic. In the examples the ceramic is Zirconia (ZrO_2) or Alumina (Al_2O_3), while the metal is Aluminium (Al). The material parameters for the metal and the ceramics are given in Table 1.

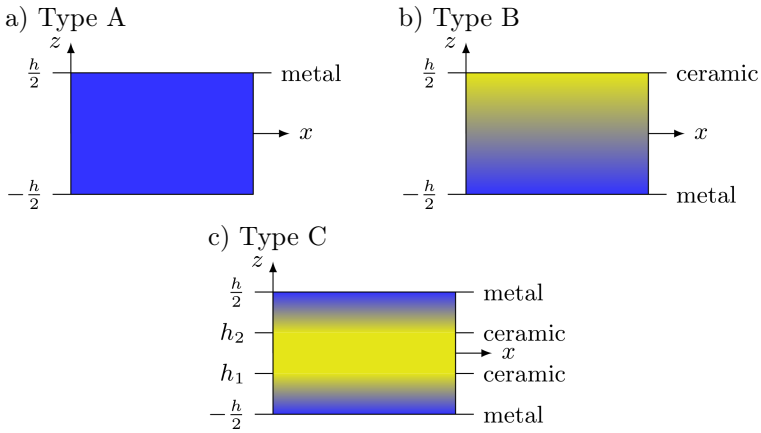

FIG. 11. Three types of transverse structures of the square plate – example 2.

Table 1. Material properties – example 2.

Material	Young's modulus [GPa]	Poisson's ratio
Aluminium (Al)	70	0.3
Zirconia (ZrO_2)	151	0.3
Alumina (Al_2O_3)	380	0.3

In the case of the plate made of FGM, Young's modulus varies continuously through the layer thickness, according to the volume fractions of the two materials. In relation to Fig. 11, the following assumed ceramic fractions for the plates of type B and C are set:

- *Type B:*

$$V_c(z) = \left(\frac{2z+h}{2h}\right)^p, \tag{7.1}$$

where p is the power index; h is the total plate thickness and $z \in \left[-\frac{h}{2}, \frac{h}{2}\right]$.

- *Type C:*

$$V_c(z) = \begin{cases} \left(\dfrac{z+\frac{h}{2}}{h_1+\frac{h}{2}}\right)^p & \text{for} \quad z \in \left[-\dfrac{h}{2}, h_1\right), \\ 1 & \text{for} \quad z \in [h_1, h_2], \\ \left(\dfrac{z-\frac{h}{2}}{h_2-\frac{h}{2}}\right)^p & \text{for} \quad z \in \left(h_2, \dfrac{h}{2}\right], \end{cases} \tag{7.2}$$

where $-\frac{h}{2} \leq h_1 \leq h_2 \leq \frac{h}{2}$.

Using the volume fraction of ceramic material V_c, effective FGM properties ($P = E$ or μ) are calculated using the rule:

$$P(z) = (P_c - P_m)V_c(z) + P_m, \tag{7.3}$$

where P_c and P_m are the appropriate material properties of the ceramic and the metal, respectively.

In the example, the FEM23 results are compared with the result obtained by a standard 3D analysis performed in Abaqus, as well as with those published in [22]. Additionally, the homogeneous plate has been analysed using the Mindlin-Reissner plate theory. In the paper [22] the 2D higher-order shear deformation theory has been applied for modelling of FG sandwich plates. The mixed interpolation of tensorial component (MITC) approach is used to solve the problem and a special finite element has bee applied with seven degrees of freedom per node.

For the simply supported plate ("SSSS" case), two versions of boundary conditions are considered for FEM23. In the first version, called FEM23-m, the boundary condition is defined in the middle surface of the plate, whereas in the second one, FEM23-l, the boundary condition is defined on the lowest surface.

Table 2 presents the results for the plate of type A (homogeneous) under uniform loading q_0. The listed results represent the normalized displacements at the plate's centre for various degrees of slenderness. Comparing the results, it can be noticed that for the thin plate ($a/h = 1000$) and for both kinds of the boundary conditions, the values are almost the same for all methods. On the other hand, for the thick plate ($a/h = 10$), there are some differences between the 2D and 3D models. It should be noted that for the simply supported thick plate, FEM23-m and FEM23-l yield different results, where the FEM23-l results are very close to those obtained by Abaqus.

The plate of type B, see Fig. 11b, is subjected to a sinusoidal loading $p_z = q_0 \sin(x\pi/a)\sin(y\pi/a)$ and is simply supported [13]. The cross-section of the

Table 2. Normalized centre deflections $100w\left(\frac{a}{2},\frac{a}{2}\right)D/q_0a^4$, $D=Eh^3/12(1-\nu^2)$ of isotropic plate under uniform loads – example 2.

BC	Theory	a/h		
		10	100	1000
SSSS	Nguyen *et al.* [22]	0.4272	0.4064	0.4062
	Reissner-Mindlin [33]	0.4273	0.4065	0.4062
	FEM23-m	0.4603	0.4085	0.4059
	FEM23-l	0.4836	0.4085	0.4059
	ABAQUS	0.4877	0.4090	0.4062
CCCC	Nguyen *et al.* [22]	0.1505	0.1268	0.1265
	Reissner-Mindlin [33]	0.1499	0.1267	0.1265
	FEM23	0.1487	0.1257	0.1252
	ABAQUS	0.1488	0.1256	0.1252

plate is a combination of Al and Al_2O_3. In this case, the normalized stress and deflection are defined as follows:

$$\overline{\sigma}_{xx}(z) = \frac{h}{aq_0}\sigma_{xx}\left(a/2,a/2,z\right), \tag{7.4}$$

$$\overline{w} = \frac{10h^3E_c}{a^4q_0}w(a/2,a/2,0). \tag{7.5}$$

Following the paper [22], the results, shown in Table 3, are in the form of normalized stresses and displacements for various plate thicknesses and values

Table 3. Normalized membrane stress $\overline{\sigma}_{xx}$ and deflection $\overline{w}$ of Al/Al_2O_3 simply supported squared FG plate type B – example 2.

p	Method	$\overline{\sigma}_{xx}(\frac{h}{3})$			$\overline{w}$		
		a/h=4	10	100	a/h=4	10	100
1	Nguyen *et al.* [22]	0.5787	1.4825	14.894	0.7271	0.5874	0.5609
	FEM23-m	0.6809	1.5794	15.020	0.8266	0.6300	0.5655
	FEM23-l	0.7532	1.6183	15.021	1.3392	0.6835	0.5655
	ABAQUS	0.7646	1.6198	15.027	1.4998	0.6869	0.5656
4	Nguyen *et al.* [22]	0.4390	1.1719	11.862	1.1593	0.8795	0.8263
	FEM23-m	0.5468	1.2776	12.333	1.3477	0.9557	0.8342
	FEM23-l	0.5945	1.3141	12.333	2.0627	1.0302	0.8343
	ABAQUS	0.5862	1.2864	11.983	2.2332	1.0349	0.8343
10	Nguyen *et al.* [22]	0.3220	0.8730	8.8566	1.3896	1.0090	0.9332
	FEM23-m	0.4571	1.0558	10.398	1.6075	1.0981	0.9433
	FEM23-l	0.4901	1.0743	10.398	2.3332	1.1725	0.9434
	ABAQUS	0.4380	0.9476	8.9695	2.4984	1.1764	0.9434

Table 4. Normalized deflection $\overline{w}$ of Al/ZrO_2 clamped squared FG plate type C.

a/h	p	Method	1-0-1	2-1-2	2-1-1	1-1-1	2-2-1	1-2-1
5	0	Nguyen *et al.* [22]	0.1652	0.1652	0.1652	0.1652	0.1652	0.1652
		FEM23-l	0.1622	0.1622	0.1622	0.1622	0.1622	0.1622
		ABAQUS	0.1622	0.1622	0.1621	0.1622	0.1622	0.1622
	0.5	Nguyen *et al.* [22]	0.2166	0.2080	0.2049	0.2019	0.1981	0.1939
		FEM23-l	0.2122	0.2038	0.2011	0.1978	0.1944	0.1900
		ABAQUS	0.2122	0.2037	0.2010	0.1977	0.1943	0.1898
	1	Nguyen *et al.* [22]	0.2496	0.2351	0.2297	0.2248	0.2182	0.2111
		FEM23-l	0.2451	0.2307	0.2260	0.2205	0.2145	0.2070
		ABAQUS	0.2451	0.2306	0.2260	0.2204	0.2144	0.2069
	10	Nguyen *et al.* [22]	0.3346	0.3046	0.2924	0.2856	0.2709	0.2581
		FEM23-l	0.3326	0.3054	0.2957	0.2841	0.2708	0.2546
		ABAQUS	0.3326	0.3053	0.2955	0.2839	0.2707	0.2543
10	0	Nguyen *et al.* [22]	0.1156	0.1156	0.1156	0.1156	0.1156	0.1156
		FEM23-l	0.1159	0.1159	0.1159	0.1159	0.1159	0.1159
		ABAQUS	0.1159	0.1159	0.1159	0.1159	0.1159	0.1158
	0.5	Nguyen *et al.* [22]	0.1588	0.1525	0.1497	0.1477	0.1442	0.1410
		FEM23-l	0.1590	0.1527	0.1500	0.1479	0.1446	0.1411
		ABAQUS	0.1589	0.1526	0.1497	0.1478	0.1443	0.1407
	1	Nguyen *et al.* [22]	0.1862	0.1760	0.1709	0.1679	0.1619	0.1563
		FEM23-l	0.1868	0.1766	0.1716	0.1684	0.1625	0.1567
		ABAQUS	0.1868	0.1765	0.1716	0.1684	0.1625	0.1567
	10	Nguyen *et al.* [22]	0.2429	0.2312	0.2204	0.2196	0.2067	0.1983
		FEM23-l	0.2446	0.2337	0.2235	0.2213	0.2088	0.1993
		ABAQUS	0.2446	0.2334	0.2234	0.2212	0.2087	0.1992
100	0	Nguyen *et al.* [22]	0.0961	0.0961	0.0961	0.0961	0.0961	0.0961
		FEM23-l	0.0992	0.0992	0.0992	0.0992	0.0992	0.0992
		ABAQUS	0.0994	0.0995	0.0995	0.0995	0.0995	0.0995
	0.5	Nguyen *et al.* [22]	0.1356	0.1302	0.1275	0.1259	0.1226	0.1196
		FEM23-l	0.1398	0.1344	0.1315	0.1300	0.1266	0.1235
		ABAQUS	0.1393	0.1341	0.1313	0.1299	0.1266	0.1235
	1	Nguyen *et al.* [22]	0.1601	0.1516	0.1468	0.1445	0.1389	0.1339
		FEM23-l	0.1658	0.1571	0.1520	0.1497	0.1438	0.1386
		ABAQUS	0.1662	0.1576	0.1524	0.1501	0.1442	0.1390
	10	Nguyen *et al.* [22]	0.2061	0.2005	0.1905	0.1915	0.1797	0.1728
		FEM23-l	0.2130	0.2080	0.1975	0.1988	0.1864	0.1795
		ABAQUS	0.2135	0.2083	0.1980	0.1993	0.1869	0.1800

of p, see Eq. (7.1). For the thin plate, all the results for displacements are in perfect agreement, but for the thick plate, there are evident differences between the 2D [22] and 3D (FEM23, ABAQUS) models. However, it can be observed that the FEM23-m displacements are in good agreement with the Nguyen 2D model. On the other hand, the FEM23-l and Abaqus results are in mutually good agreement. There are some differences in stresses, especially for higher values of the parameter p. This may be caused by different smoothing procedures applied in those methods.

Both the model used by Nguyen *et al.* in [22] and the Reissner-Mindlin model used in [33] are good for thin plates. For thick plates, such as in the cases $a/h = 4$ and $a/h = 10$, the both models give results with less accuracy, what can be observed in the Tables 2 and 3.

A square plate, now made of Al/ZrO_2 with a cross section type C, see Fig. 11c, under a sinusoidal load, has been subsequently computed. The results in the form of normalized deflections for different thickness ratios of the plate are listed in Table 4. Following paper [22], various configurations of three layers are considered. The configurations are coded as $a - b - c$, where a, b and c indicate the relative thickness of the following layers.

In this case, the agreement of the results obtained by FEM23-l and Abaqus can be observed. The results of the 2D model by Nguyen *et al.* [22] are different, in comparison to those obtained by the 3D models, both for thick and for thin plates.

8. Conclusions

In this paper, we have presented effective numerical method, FEM23, used to analyse layered plates made of functionally graded materials. In FEM23, the plate may be a single-layer or a multi-layered laminate, where some layers can be made of FGM. FEM23 uses only a 2D mesh, but full 3D results are obtained for laminated plates, which may consist of thin and thick layers. It has been assumed in this paper that the material properties may change only in direction z (the transverse direction). FEM23 uses a special spatial approximation which is a combination of the 1D transverse and the 2D in-plane approximations which are identical as the approximations of 3D-based hierarchical plate and shell models. For each of the layers, the transverse approximation order can be set independently and adequately to the layer thickness and the level of the material change. Furthermore, the Gauss-Legendre transverse integration quadrature may be adjusted to suit the needs of each particular case.

This paper discusses two examples. In the first example, bending of a sandwich beam with an FG core has been considered. The second example involves bending of a square plate. The plate is either homogeneous or layered, with

some layers composed of FGM. The accuracy of FEM23 has been demonstrated in these examples, as the FEM23 results have been compared to other known results from literature or those obtained by the standard 3D FEM analysis.

References

1. Byfut A., Schröder A., Unsymmetric multi-level hanging nodes and anisotropic polynomial degrees in h1-conforming higher-order finite element methods, *Computers & Mathematics with Applications*, **73**(9): 2092–2150, 2017, doi: /10.1016/j.camwa.2017.02.029.

2. Carrera E., c^0 Reissner-Mindlin multilayered plate elements including zig-zag and interlaminar stress continuity, *International Journal for Numerical Methods in Engineering*, **39**(11): 1797–1820, 1996, doi: 10.1002/(SICI)1097-0207(19960615)39:11<1797::AID-NME928>3.0.CO;2-W.

3. Carrera E., Historical review of Zig-Zag theories for multilayered plates and shells, *ASME Applied Mechanics Reviews*, **56**(3): 287–308, 2003, doi: 10.1115/1.1557614.

4. Carrera E., Cinefra M., Li G., Refined finite element solutions for anisotropic laminated plates, *Composite Structures*, **183**: 63–76, 2018, doi: 10.1016/j.compstruct.2017.01.014.

5. Carrera E., Kröplin B., Zigzag and interlaminar equilibria effects in large-deflection and postbuckling analysis of multilayered plates, *Mechanics of Composite Materials and Structures*, **4**(1): 69–94, 1997, doi: 10.1080/10759419708945875.

6. Di Sciuva M., An improved shear-deformation theory for moderately thick multilayered anisotropic shells and plates, *ASME Journal of Applied Mechanics*, **54**(3): 589–596, 1987, doi: 10.1115/1.3173074.

7. Fallah N., Delzendeh M., Free vibration analysis of laminated composite plates using meshless finite volume method, *Engineering Analysis with Boundary Elements*, **88**: 132–144, 2018, doi: 10.1016/j.enganabound.2017.12.011.

8. Ferreira A.J.M., Analysis of composite plates using a layerwise theory and multiquadrics discretization, *Mechanics of Advanced Materials and Structures*, **12**(2): 99–112, 2005, doi: 10.1080/15376490490493952.

9. Ferreira A., Carrera E., Cinefra M., Roque C., Polit O., Analysis of laminated shells by a sinusoidal shear deformation theory and radial basis functions collocation, accounting for through-the-thickness deformations, *Composites Part B: Engineering*, **42**(5): 1276–1284, 2011, doi: 10.1016/j.compositesb.2011.01.031.

10. Filippi M., Carrera E., Zenkour A., Static analyses of fgm beams by various theories and finite elements, *Composites Part B: Engineering*, **72**: 1–9, 2015, doi: 10.1016/j.compositesb.2014.12.004.

11. Golubović A., Demirdžić I., Muzaferija S., Finite volume analysis of laminated composite plates, *International Journal for Numerical Methods in Engineering*, **109**(11): 1607–1620, 2017, doi: 10.1002/nme.5347.

12. Jaśkowiec J., Pluciński P., Three-dimensional modelling of heat conduction in laminated plate by two-dimensional numerical model, *Composite Structures*, **171**: 562–575, 2017, doi: 10.1016/j.compstruct.2017.03.046.

13. Jaśkowiec J., Pluciński P., Stankiewicz A., Cichoń C., Three-dimensional modelling of laminated glass bending on two-dimensional in-plane mesh, *Composites Part B: Engineering*, **120**: 63–82, 2017, doi: 10.1016/j.compositesb.2017.03.008.

14. Jha D., Kant T., Singh R., A critical review of recent research on functionally graded plates, *Composite Structures*, **96**: 833–849, 2013, doi: 10.1016/j.compstruct.2012.09.001.

15. Kulikov G.M., Plotnikova S.V., Mamontov A.A., Sampling surfaces formulation for thermoelastic analysis of laminated functionally graded shells, *Meccanica*, **51**(8): 1913–1929, 2016, doi: /10.1007/s11012-015-0347-1.

16. Kulikov G.M., Plotnikova S.V., Three-dimensional exact analysis of functionally graded laminated composite plates, [in:] Altenbach H., Mikhasev G.I. [Eds], *Shell and Membrane Theories in Mechanics and Biology: From Macro- to Nanoscale Structures*, pp. 223–241, *Springer International Publishing*, Cham, 2015, doi: 10.1007/978-3-319-02535-3_13.

17. Kulikov G.M., Plotnikova S.V., On the use of sampling surfaces method for solution of 3D elasticity problems for thick shells, *ZAMM – Journal of Applied Mathematics and Mechanics/Zeitschrift für Angewandte Mathematik und Mechanik*, **92**(11–12): 910–920, 2012, doi: 10.1002/zamm.201200028.

18. Kulikov G.M., Plotnikova S.V., Heat conduction analysis of laminated shells by a sampling surfaces method, *Mechanics Research Communications*, **55**: 59–65, 2014, doi: 10.1016/j.mechrescom.2013.10.018.

19. Kulikov G.M., Plotnikova S.V., Strong sampling surfaces formulation for layered shells, *International Journal of Solids and Structures*, **121**: 75–85, 2017, doi: 10.1016/j.ijsolstr.2017.05.017.

20. Liu B., Ferreira A.J.M., Xing Y.F., Neves A.M.A., Analysis of functionally graded sandwich and laminated shells using a layerwise theory and a differential quadrature finite element method, *Composite Structures*, **136**: 546–553, 2016, doi: 10.1016/j.compstruct.2015.10.044.

21. Naebe M., Shirvanimoghaddam K., Functionally graded materials: A review of fabrication and properties, *Applied Materials Today*, **5**: 223–245, 2016, doi: 10.1016/j.apmt.2016.10.001.

22. Nguyen T.-K., Nguyen V.-H., Chau-Dinh T., Vo T.P., Nguyen-Xuan H., Static and vibration analysis of isotropic and functionally graded sandwich plates using an edge-based MITC3 finite elements, *Composites Part B*, **107**: 162–173, 2016, doi: 10.1016/j.compositesb.2016.09.058.

23. Pandey S., Pradyumna S., Free vibration of functionally graded sandwich plates in thermal environment using a layerwise theory, *European Journal of Mechanics – A/Solids*, **51**: 55–66, 2015, doi: 10.1016/j.euromechsol.2014.12.001.

24. Pandey S., Pradyumna S., A layerwise finite element formulation for free vibration analysis of functionally graded sandwich shells, *Composite Structures*, **133**: 438–450, 2015, doi: 10.1016/j.compstruct.2015.07.087.

25. Pandey S., Pradyumna S., Transient stress analysis of sandwich plate and shell panels with functionally graded material core under thermal shock, *Journal of Thermal Stresses*, **41**(5): 543–567, 2018, doi: 10.1080/01495739.2017.1422999.

26. Rachowicz W., Pardo D., Demkowicz L., Fully automatic *hp*-adaptivity in three dimensions, *Computer Methods in Applied Mechanics and Engineering*, **195**(37): 4816–4842, 2006, doi: 10.1016/j.cma.2005.08.022.

27. Rachowicz W., Zdunek A., An *h*-adaptive mortar finite element method for finite deformation contact with higher order *p* extension, *Computers & Mathematics with Applications*, **73**(8): 1834–1854, 2017, doi: 10.1016/j.camwa.2017.02.022.

28. Reddy J.N., Mechanics of laminated composite plates and shells: theory and analysis, 2nd Ed., *Taylor & Francis*, 2004.

29. Ren J., A new theory of laminated plate, *Composites Science and Technology*, **26**(3): 225–239, 1986, doi: 10.1016/0266-3538(86)90087-4.

30. Swaminathan K., Naveenkumar D.T., Zenkour A.M., Carrera E., Stress, vibration and buckling analyses of FGM plates – a state-of-the-art review, *Composite Structure*, **120**: 10–31, 2015, doi: 10.1016/j.compstruct.2014.09.070.

31. Swaminathan K., Sangeetha D.M., Thermal analysis of FGM plates – A critical review of various modeling techniques and solution methods, *Composite Structures*, **160**: 43–60, 2017, doi: 10.1016/j.compstruct.2016.10.047.

32. Szabó B.A., Sahrmann G.J., Hierarchic plate and shell models based on p-extension, *International Journal for Numerical Methods in Engineering*, **26**(8): 1855–1881, 1988, doi: 10.1002/nme.1620260812.

33. Taylor R.L., Auricchio F., Linked interpolation for Reissner-Mindlin plate elements: Part II – A simple triangle, *International Journal for Numerical Methods in Engineering*, **36**(18): 3057–3066, 1993, doi: 10.1002/nme.1620361803.

34. Zappino E., Carrera E., Refined One-Dimensional Models for the Multi-Field Analysis of Layered Smart Structures, pp. 343–366, *Springer Singapore*, Singapore, 2018.

35. Zboiński G., Application of the three-dimensional triangular-prism hpq adaptive finite element to plate and shell analysis, *Computers & Structures*, **65**(4): 497–514, 1997, doi: 10.1016/S0045-7949(96)00415-4.

36. Zboiński G., Hierarchical modeling and finite element approximation for adaptive analysis of complex structures, *DSc Thesis*, Gdańsk (Poland), 2001.

37. Zboiński G., 3D-based *hp*-adaptive first order shell finite element for modelling and analysis of complex structures – Part 2: Application to structural analysis, *International Journal for Numerical Methods in Engineering*, **70**(13): 1546–1580, 2007, doi: 10.1002/nme.1919.

38. Zboiński G., Adaptive hpq finite element methods for the analysis of 3D-based models of complex structures. Part 1. Hierarchical modeling and approximations estimation, *Computer Methods in Applied Mechanics and Engineering*, **1999**(45–48): 2913–2940, 2010, doi: 10.1016/j.cma.2010.06.003.

39. Zboiński G., Adaptive hpq finite element methods for the analysis of 3D-based models of complex structures. Part 2. A posteriori error estimation, *Computer Methods in Applied Mechanics and Engineering*, **267**: 531–565, 2013, doi: 10.1016/j.cma.2013.08.018.

40. Zboiński G., Jasiński M., 3D-based *hp*-adaptive first-order shell finite element for modelling and analysis of complex structures – Part 1: The model and the approximation,

International Journal for Numerical Methods in Engineering, **70**(13): 1513–1545, 2007, doi: 10.1002/nme.1920.

41. Zienkiewicz O.C., Zhu J.Z., The superconvergent patch recovery and a posteriori error estimates. Part 1: The recovery technique, *International Journal for Numerical Methods in Engineering*, **33**(7): 1331–1364, 1992, doi: 10.1002/nme.1620330702.

42. Zienkiewicz O.C., Zhu J.Z., The superconvergent patch recovery and a posteriori error estimates. Part 2: Error estimates and adaptivity, *International Journal for Numerical Methods in Engineering*, **33**(7): 1365–1382, 1992, doi: 10.1002/nme.1620330703.

Received May 31, 2019; accepted version August 19, 2019.

Published on Creative Common licence CC BY-SA 4.0